J. Fluid Mech. (1991), *vol.* 226, *pp.* 291–317
Printed in Great Britain

Potential flow solution for a yawed surface-piercing plate

By HONGBO XÜ

Department of Ocean Engineering, Massachusetts Institute of Technology, Cambridge, MA 02139, USA

(Received 28 December 1989 and in revised form 19 September 1990)

This paper presents the results of an analytical investigation of the steady translation of a vertical surface-piercing plate at a small angle of attack. This problem is the antisymmetric equivalent of the symmetric thin-ship problem solved by Michell. The linearized boundary-value problem is transformed into an integral equation of the first kind by the method of Green functions. The Kelvin–Havelock Green function is used to satisfy the linearized free-surface boundary condition and radiation condition. A pressure Kutta condition is imposed at the trailing edge. Effective algorithms are developed to evaluate the hypersingular kernel without recourse to numerical integration. The resulting integral equation is solved by a collocation method with a refined scheme of discretization. After establishing the convergence of the present algorithm, computations are carried out for a surface-piercing rectangular plate of aspect ratio 0.5. The integrated lateral-force and yaw-moment coefficients show good agreement with experimental data. Other parameters of the flow such as pressure distributions, drag, strength of leading-edge singularity and free-surface profiles on the plate are also presented. The incompatibility between the pressure Kutta condition and the linearized free-surface condition does not affect the global solution.

1. Introduction

As in the analogous thin-wing problem, steady potential flow past a surface-piercing lifting body at a small angle of attack can be decomposed into two portions: a thickness problem and a lifting problem. The former corresponds to the flow past a symmetrical body at zero angle of attack. The latter corresponds to the effects of camber and angle of attack for a lifting surface of zero thickness. Within the scope of the linearized potential theory, the thickness problem can be solved by a suitable source distribution on the plane of symmetry, in exactly the same manner as for the classical thin-ship theory developed by Michell (1898). However, the solution of the corresponding lifting problem which combines the complexity of lifting surfaces and ship waves was not well understood. The present work focuses on the lifting problem. From a practical point of view, the solution of the lifting problem is essential in studying a sailboat on a tack, a thin ship in manoeuvering, a surface-piercing strut on a hydrofoil boat, or a demihull of a twin-hull vessel.

The mathematical difficulties of the lifting problem arise primarily from the presence of singularities at edges of a lifting surface and in the kernel of the corresponding integral equation. Since the intersection with the free surface is the confluence line of the linearized free-surface boundary condition and the body

condition, difficulties are anticipated there. However, since the wave effects attenuate vertically, a square-root singularity exists at the lower edge, similar to the thin-wing problem. From a coordinate transfer, it is clear that the pressure distribution on a surface-piercing lifting body with zero thickness has a square-root infinity at the leading edge, and a removable singularity at the trailing edge. Moreover, a finite jump of the free-surface elevation across the trailing edge is often observed in experiments especially at high Froude numbers (see van den Brug, Beukelman & Prince 1971). This discontinuity manifests the strong nonlinearity of the free-surface flow in the vicinity of the trailing edge.

The earlier works on the subject used either an integral equation formulation or a slender-body approximation. Newman (1961) used a dipole distribution to represent a rectangular surface-piercing strut and derived an integral equation for the dipole strength. A similar formulation was adopted by Daoud (1973), but his solution scheme suffered numerical instability. Kern (1973) studied the design problem also using an integral formulation.

One of the main motivations of studying the lifting problem is to understand the flow in a bow region, e.g. local cavitation and separation. This requires knowledge of the spanwise distribution of the parameter associated with the square-root singularity at the leading edge. A local analysis at the leading edge based on the assumption that the spanwise distribution of load is elliptical was presented by Newman (1973). However, the solution is valid only when free-surface effects are not important.

Studies based on the assumption of small aspect ratio have been reported by Hirata (1975) and Chapman (1976). In the study carried out by Chapman, the longitudinal coordinate was treated as a time-like variable, and the steady three-dimensional problem was restated in the form of unsteady two-dimensional flow in the transverse plane with time advance corresponding to translation of the solution plane aft. The resulting problem was solved by a finite-difference scheme which discretizes the flow field near the plate into square grids and matches the near-field solution with the far-field solution on the outer boundary. Chapman illustrated, using the special case of the leading edge, that the vertical velocity component for a yawed plate has a square-root singularity at the lower edge and a logarithmic singularity at the intersection with the free surface. He also extended his method to satisfy the nonlinear free-surface boundary conditions. In general, Chapman's slender-body approach is valid for high Froude numbers. Other limitations are (i) the effects of transverse waves are completely ignored, (ii) the equally spaced grid mesh is not suitable for a solution known to have a square-root singularity at the edges of the domain, (iii) the validity of the method is not justified in the vicinity of the leading edge. The example case analysed by Hirata (1975) using a Fourier transform method appears to be equivalent to the linear problem studied by Chapman. However, his calculated free-surface elevation in the region near the bow seems quite different from Chapman's.

In the present study, a rectangular plate of zero thickness is selected as the lifting model. In spite of its simple geometry, it embodies most of the fundamental features associated with the lifting problem. The boundary-integral-equation formulation is employed since it has fewer unknowns than volume discretizations. The Kelvin–Havelock Green function is used to satisfy the linearized free-surface condition and radiation condition. By applying Green's theorem, the solution of the linearized boundary-value problem is replaced by the boundary integrals on the centreplane and its wake. Thus, the problem is reduced to the solution of an integral equation of

the first kind subject to a Kutta condition at the trailing edge and a condition of continuous pressure across the wake.

Since the flow in this linear problem is antisymmetric with respect to the transverse coordinate, the free-surface elevation alongside the centreplane downstream to the trailing edge may have a finite difference. Even though this appears consistent with the observations of the free-surface jump phenomenon behind the trailing edge, it is not consistent with the underlying assumptions of linearizing the problem: free-surface elevation is continuous and the wave slope is small. In this study, the pressure Kutta condition is imposed at the trailing edge. This condition together with the condition on the wake sheet ensures that the free-surface elevation is continuous across the wake. However, it is found that in the linearized formulation the pressure Kutta condition is not compatible with the linear free-surface condition. As a consequence of this, a non-uniformity occurs near the intersection point of the trailing edge and the free surface, but it is a local phenomenon.

In §3, the solution scheme for the integral equation is developed based on a collocation method in which the continuous dipole distribution is approximated by piecewise-constant dipole panels. In view of the singularities at the edges, the two-dimensional theory introduced by Lan (1974) for thin wings is generalized to discretize the surface-piercing plate. The expansions and algorithms for evaluating the derivatives of the Green function are derived based on the efficient expansions of the Green function itself derived by Newman (1986, 1987*a*, *b*). The convergence of the present numerical scheme is established by systematically refining the discretizations and comparing results with other known solutions in the limiting case of zero Froude number. All major hydrodynamic coefficients of the flow are expressed in terms of the dipole density function. The pressure distributions over the entire domain of a lifting surface are computed for various Froude numbers. Special attention is given to the behaviour of the singularity at the leading edge to study the local cross-flow effects. The free-surface profiles on the centreplane of a lifting body are also presented. The present results are compared with experimental data by van den Brug *et al.* and other theoretical results. The extension of the present approach to other geometric forms of a plate is also discussed.

2. Mathematical formulation

A vertical rectangular surface-piercing plate of zero thickness, moving with constant velocity U and a small angle of attack α, is considered. Cartesian coordinates (x, y, z) are selected with the origin at the intersection of the trailing edge and the waterline, the x-axis in the direction of forward motion of the plate, the y-axis positive downwards. The plane $y = 0$ coincides with the undisturbed position of the free surface. The geometry of the plate and the coordinate system are shown in figure 1. The submerged portion of the lifting surface has a span s and a chord length c. No restriction on the aspect ratio s/c is made.

It is assumed that the fluid is inviscid and incompressible, and the flow is irrotational except on the lifting surface and its wake. Thus, the perturbation velocity potential ϕ must satisfy the Laplace equation

$$\nabla^2\phi = 0 \tag{1}$$

in the fluid domain excluding the wake sheet.

Neither separation nor cavitation are included in this formulation. Since the angle of attack is assumed small, the kinematic and dynamic boundary conditions on the

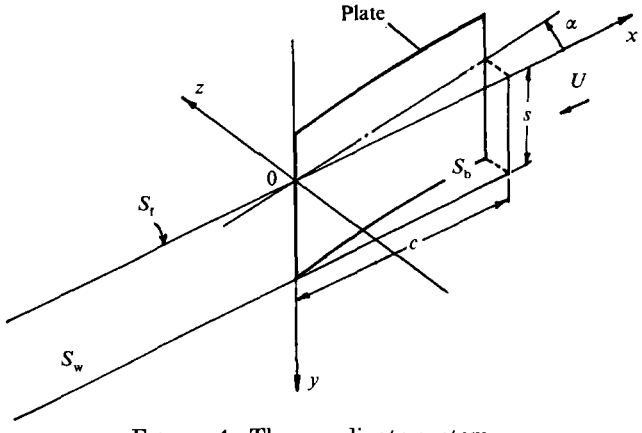

FIGURE 1. The coordinate system.

free surface may be linearized and combined to be satisfied on the undisturbed free surface S_f, namely,

$$\frac{\partial^2\phi}{\partial x^2}-K\frac{\partial\phi}{\partial y}=0 \quad \text{on} \quad y=0, \tag{2}$$

where $K=g/U^2$ is the wavenumber of a plane progressive wave with the phase speed U and g is the gravitational acceleration. If the slope of the camber is uniformly small, the kinematic body boundary condition may also be linearized and satisfied on the centreplane S_b ($0\leqslant x\leqslant c$; $0\leqslant y\leqslant s$). This condition can be written as

$$\frac{\partial\phi}{\partial z}=U\left(\alpha-\frac{\partial f(x,y)}{\partial x}\right) \quad \text{on} \quad z=0, \tag{3}$$

where $f(x,y)$ is the function of the mean-camber surface.

Neglecting the velocity-squared terms in Bernoulli's equation, the pressure in the fluid is given by

$$p^{\pm}-p_a=\rho U\frac{\partial\phi^{\pm}}{\partial x}+\rho gy, \tag{4}$$

where ρ is the density of fluid, p_a is the pressure on the free surface, and the superscripts denote the limiting values as $z\to 0^{\pm}$. On physical grounds, the pressure must be continuous across the wake, i.e. $\Delta p=p^+-p^-=0$ on the wake

$$S_w\ (-\infty<x<0;\ 0\leqslant y\leqslant s).$$

This gives the following condition:

$$\frac{\partial}{\partial x}(\phi^+-\phi^-)=0. \tag{5}$$

For large water depth the velocity must vanish at the bottom. That is

$$\nabla\phi\to 0 \quad \text{as} \quad y\to\infty. \tag{6}$$

The boundary-value problem is completed by including a radiation condition which specifies that there are only waves downstream of the disturbance, and a Kutta condition at the trailing edge which requires that the velocity remains finite and

continuous at the trailing edge. From the Kutta condition it is deduced that the pressure on the two sides of the trailing edge should have the same finite limit. Thus, the condition (5) can be extended to $x = 0$.

From the linearized Bernoulli's equation, the free-surface elevation is given by

$$\eta_f = -\frac{U}{g}\frac{\partial\phi}{\partial x}\bigg|_{y=0}. \tag{7}$$

Since the only inhomogeneity is on S_b and the potential function is odd in z, (5) and (7) imply that the free-surface elevation is uniformly zero on the centreplane, except on S_b where it changes sign across the plate. Hence, longitudinally the free-surface elevation at the intersection with the trailing edge may be discontinuous unless it happens to be zero. Therefore, at the intersection point of the free surface and trailing edge, which is a confluence of the Kutta condition, linearized free-surface condition, body condition and wake condition, the conditions of zero pressure difference on the trailing edge (pressure Kutta condition) and continuous free-surface elevation are not compatible. This is clearly a consequence of linearization. Nevertheless, it is plausible that the difficulty at the intersection point will not ruin the global solution if all conditions are properly satisfied elsewhere.

The above boundary-value problem can be solved by applying the method of Green functions. Defining a field point $\boldsymbol{p} = (x, y, z)$ and a unit singularity point $\boldsymbol{q} = (\xi, \eta, \zeta)$, the Green function corresponding to the above boundary-value problem, which satisfies (1), (2), (6) and the radiation condition can be written in the following form:

$$G(\boldsymbol{p}, \boldsymbol{q}) = \frac{1}{r} - \frac{1}{r_0} + H(\boldsymbol{p}, \boldsymbol{q}), \tag{8}$$

where r and r_0 are, respectively, the distances from a field point to the singularity point and its image above the free surface:

$$\left.\begin{aligned} r &= [(x-\xi)^2 + (y-\eta)^2 + (z-\zeta)^2]^{\frac{1}{2}}, \\ r_0 &= [(x-\xi)^2 + (y+\eta)^2 + (z-\zeta)^2]^{\frac{1}{2}}, \end{aligned}\right\} \tag{9}$$

and with the harmonic function $H(\boldsymbol{p}, \boldsymbol{q})$ represents the effects due to the free surface, which satisfies the linear free-surface condition and radiation condition.

If Green's theorem is applied to the control volume which is bounded by S_f, S_b, S_w and a far-field closure, it can be shown that the only contributions are from S_b and S_w, which give the velocity potential ϕ in the fluid domain as

$$\phi(\boldsymbol{p}) = -\frac{1}{4\pi}\iint_{S_b^+ \cup S_w^+} [\phi(\xi, \eta, 0^+) - \phi(\xi, \eta, 0^-)]\frac{\partial G}{\partial n}\,\mathrm{d}\xi\,\mathrm{d}\eta, \tag{10}$$

where domains S_b^+ and S_w^+ are defined as S_b and S_w in the limit of $z \to 0^+$, where $\partial G/\partial n = \partial G/\partial z = -\partial G/\partial\zeta$. Letting $m(\xi, \eta) = \phi(\xi, \eta, 0^+) - \phi(\xi, \eta, 0^-)$, equation (10) expresses the velocity potential in terms of a continuous normal dipole distribution over the lifting surface and its wake with the unknown strength $m(\xi, \eta)$. Differentiating both sides of this equation with respect to z, and imposing the boundary condition (3) on S_b, the resulting equation may be written as

$$\frac{1}{4\pi}\lim_{z\to 0}\frac{\partial}{\partial z}\iint_{S_b^+ \cup S_w^+} m(\xi, \eta)\frac{\partial G}{\partial\zeta}\bigg|_{\zeta=0}\mathrm{d}\xi\,\mathrm{d}\eta = U\left(\alpha - \frac{\partial f(x, y)}{\partial x}\right). \tag{11}$$

This is the Fredholm integral equation of the first kind to be solved for the unknown function $m(x, y)$. It must be noted that the order of the integration and differentiation in (11) can *not* be arbitrarily interchanged. Otherwise, it will lead to a mathematically ill-defined integral equation.

From (5), the unknown $m(x, y)$ is independent of x on the wake S_w,

$$m(x, y) = m(0, y) \quad \text{for} \quad -\infty < x \leqslant 0; 0 \leqslant y \leqslant s. \tag{12}$$

Thus, the unknowns are confined within the lifting surface S_b. Moreover, since the potential is continuous outside surfaces S_b and S_w, the potential jump $m(x, y)$ must vanish at the leading edge and the lower edge of S_b. That is

$$\left.\begin{aligned} m(c, y) &= 0 \quad \text{for} \quad 0 \leqslant y \leqslant s, \\ m(x, s) &= 0 \quad \text{for} \quad 0 \leqslant x \leqslant c. \end{aligned}\right\} \tag{13}$$

However, no similar assumptions can be made on the waterline.

The Green function is well known in slip-wave theory, and corresponds to the velocity potential of a submerged source moving with constant horizontal speed beneath the free surface. An effective representation of this Green function given by Newman (1987*a*) is selected for its convenience in numerical applications:

$$G(\boldsymbol{p}, \boldsymbol{q}) = \frac{1}{r} - \frac{1}{r_0} + \mathrm{Re}\left[\lim_{\epsilon \to 0} \frac{2\mathrm{i}}{\pi} \int_{-\pi/2}^{\pi/2} \cos\varphi \, \mathrm{d}\varphi \int_0^{\infty} \mathrm{d}k \frac{\mathrm{e}^{v(\boldsymbol{p}, \boldsymbol{q}, \varphi, k)}}{k - K\cos^2\varphi + \mathrm{i}\epsilon} \right.$$
$$\left. + 4\mathrm{i}H(\xi - x) \int_{-\pi/2}^{\pi/2} \mathrm{d}\vartheta \sec^2\vartheta \, \mathrm{e}^{u(\boldsymbol{p}, \boldsymbol{q}, \vartheta) K}\right], \tag{14}$$

where K is the wavenumber as defined in (2), and $H(\xi - x)$ is the unit step function which is equal to 1 if $\xi > x$, 0 otherwise. Two auxiliary functions are defined by

$$v(\boldsymbol{p}, \boldsymbol{q}, \varphi, k) = -k(y + \eta) + \mathrm{i}k|x - \xi| \sec\varphi + k(z - \zeta)\tan\varphi,$$
$$u(\boldsymbol{p}, \boldsymbol{q}, \vartheta) = -(y + \eta)\sec^2\vartheta + \mathrm{i}(x - \xi)\sec\vartheta + \mathrm{i}|z - \zeta| \sec^2\vartheta \sin\vartheta,$$

where the double integral in (14) represents a symmetrical non-radiating disturbance, and the single integral accounts for the wave field downstream.

In the limits of zero or infinite Froude number, the Green function reduces to $1/r \pm 1/r_0$, respectively. The corresponding solutions to the lifting problem are equivalent to those for a double-body flow except that in the infinite-Froude-number case the image body is at a negative angle of attack.

All of the hydrodynamic coefficients can be expressed in terms of the unknown dipole density function $m(x, y)$. From the linearized Bernoulli's equation (4), the non-dimensional pressure coefficient on the lifting surface can be expressed as

$$\Delta C_p = \frac{\Delta p}{\frac{1}{2}\rho U^2} = -\frac{2}{U} \frac{\partial m(x, y)}{\partial x}. \tag{15}$$

To examine the singularities in the pressure distribution, the simplest way is through the following transformation:

$$x = \tfrac{1}{2}c(1 + \cos\theta), \tag{16}$$

where $0 \leqslant \theta \leqslant \pi$. Hence,

$$\Delta C_p = \frac{4}{Uc\sin\theta} \frac{\partial m(\theta, y)}{\partial \theta}, \tag{17}$$

where $\sin\theta = 2x^{\frac{1}{2}}(c-x)^{\frac{1}{2}}/c$. From this expression it is clear that the pressure is indeed singular at both leading and trailing edges. From (5) and (17) it also becomes clear that the physical Kutta condition of finite and continuous velocity at the trailing edge is equivalent to requiring that the pressure difference across the plate vanishes at the trailing edge. Therefore, the singularity at the trailing edge is removable. Using a similar coordinate transfer, it can be shown that the vertical velocity component is also singular at the waterline and the lower edge. The singularity at the lower edge is of square-root type, but the singularity at the waterline must be determined in the light of free-surface effects.

Assuming that the dipole density $m(\theta, y)$ is twice differentiable in θ, the pressure coefficient at the trailing edge can be expressed by

$$\Delta C_p|_{x=0} = -\frac{4}{Uc}\frac{\partial^2 m(\theta, y)}{\partial\theta^2}\bigg|_{\theta=\pi}, \tag{18}$$

where L'Hospital's rule is applied.

The strength of the square-root singularity at the leading edge is defined as

$$C(y) = \frac{1}{2c^{\frac{1}{2}}}\lim_{x\to c}\Delta C_p(c-x)^{\frac{1}{2}}. \tag{19}$$

Substituting (15) into the above expression and integrating both sides with respect to x, the parameter $C(y)$ is given by

$$C(y) = \frac{1}{2Uc^{\frac{1}{2}}}\lim_{x\to c}\frac{m(x, y)}{(c-x)^{\frac{1}{2}}}. \tag{20}$$

The magnitude of the sectional leading-edge thrust coefficient $C_t(y)$ can be calculated by

$$C_t(y) = \tfrac{1}{2}\pi C^2(y) \tag{21}$$

and the total thrust coefficient at the leading edge can be computed by

$$C_T = \frac{\pi}{2s}\int_0^s C^2(y)\,\mathrm{d}y. \tag{22}$$

Integrating the pressure jump along the chord from the leading edge to the trailing edge yields the sectional lateral-force coefficients,

$$C_l(y) = \frac{1}{c}\int_0^c \Delta C_p\,\mathrm{d}x = \frac{2m(0, y)}{Uc}, \tag{23}$$

where condition (13) is imposed. The total lateral-force coefficient $C_L = L/(1/2\rho U^2 S_0)$ can be obtained by integrating the sectional coefficient along the spanwise direction:

$$C_L = \frac{1}{s}\int_0^s C_l(y)\,\mathrm{d}y = \frac{2}{US_0}\int_0^s m(0, y)\,\mathrm{d}y, \tag{24}$$

where $S_0 = sc$ is the area of the submerged portion of the lifting surface. The accumulative lateral-force coefficient $C_l(x)$ is defined as the total lateral-force coefficient from the leading edge to a longitudinal section at x, that is

$$C_l(x) = \frac{1}{S_0}\int_0^s\int_0^x \Delta C_p\,\mathrm{d}x'\,\mathrm{d}y = \frac{2}{US_0}\int_0^s m(x, y)\,\mathrm{d}y. \tag{25}$$

The sectional yaw-moment coefficient with respect to the mid-chord point is given by

$$C_m(y) = \frac{2}{c^2}\int_0^c \Delta C_p(\tfrac{1}{2}c - x)\,\mathrm{d}x$$

$$= \frac{m(0,y)}{Uc} - \frac{2}{Uc^2}\int_0^c m(x,y)\,\mathrm{d}x. \tag{26}$$

The total yaw-moment coefficient $C_M = M/(1/2\rho U^2 S_0 c)$ can thus be obtained by integrating the above coefficient along the spanwise direction:

$$C_m = \frac{1}{s}\int_0^s C_m(y)\,\mathrm{d}y$$

$$= \frac{1}{US_0}\int_0^s m(0,y)\,\mathrm{d}y - \frac{2}{US_0 c}\int_0^s\int_0^c m(x,y)\,\mathrm{d}x\,\mathrm{d}y. \tag{27}$$

The total yaw-moment coefficient with respect to the leading edge can be evaluated from the relation

$$C'_M = \tfrac{1}{2}C_L + C_M. \tag{28}$$

The sectional near-field induced drag can be computed by

$$C_d^{(1)}(y) = C_l(y)\,\alpha - C_t(y) \tag{29}$$

and the total drag coefficient $C_D^{(1)} = D/(1/2\rho U^2 S_0)$ is given by

$$C_D^{(1)} = C_L\,\alpha - C_T. \tag{30}$$

Finally, since the potential function is odd in z, the free-surface profile on the pressure side of the plate can be expressed in terms of the limiting values of the pressure coefficient on the waterline:

$$\eta_f(x, z=0) = \tfrac{1}{4}cF_n^2\,\Delta C_p|_{y=0}, \tag{31}$$

where $0 \leqslant x \leqslant c$.

3. Numerical implementation

Since the integral equation (11) cannot be solved analytically, our attention in this section is focused on its numerical solution by a panel method. The domain of the surface integration is discretized into a number of quadrilateral panels. The dipole density is assumed constant on each panel and the strength is to be determined by collocation. Thus, the continuous dipole distribution in (11) is approximated by a discrete one. If the numerical scheme is convergent, the difference between the numerical solution and the continuous limit can be made arbitrarily small with a sufficient number of panels.

The effectiveness of this approach, in this case, depends on (i) a discretization scheme which takes the singularities at the edges of S_b into account; (ii) the efficient algorithm for evaluating the kernel function throughout the centreplane. In view of the similarity to the thin-wing problem, several schemes of discretization are modified from either the vortex-lattice method (VLM) (cf. Hough 1973) or the quasi-continuous method (QCM) by Lan (1974). The following scheme is selected for its superior convergence property, which is a generalization of the QCM.

It has been demonstrated by Lan in a two-dimensional case that the downwash integral can be reduced to a finite sum through the Gauss–Chebyshev quadrature in

spite of the square-root singularity in the vortex density and the Cauchy singularity in the kernel. In the present study, this conclusion has been applied in both the chordwise and spanwise directions. Thus the collocation sections in both the longitudinal (chordwise) and vertical (spanwise) directions are selected at the zeros of the Chebyshev polynomial of the first kind. The panels are arranged such that each collocation point corresponds to the centroid of a panel in the θ-coordinate, which is defined in (16). Based on the concept described above, the chordwise locations of the panel edges on S_b are selected at

$$\left.\begin{aligned} x_i &= \tfrac{1}{2}c\left(1+\cos\left[(2i-1)\frac{\pi}{2N}\right]\right), \\ x_{N+1} &= -\tfrac{1}{2}c\left(1-\cos\frac{\pi}{2N}\right), \end{aligned}\right\} \tag{32}$$

where $i = 1, 2, \ldots, N$ and N is the number of longitudinal panel segments on S_b. The collocation section on each panel segment is located at

$$x_i^c = \tfrac{1}{2}c\left(1+\cos\frac{i\pi}{N}\right) \quad \text{where} \quad i = 1, 2, \ldots, N, \tag{33}$$

where the last collocation section is placed on the trailing edge. It must be noted that satisfying the body boundary condition on the trailing edge ensures that the wake leaves the trailing edge smoothly. The Kutta condition is fulfilled numerically by putting in a constant panel which overlaps the trailing edge.

In the spanwise direction, a similar choice of the panel strip and collocation section is used. The locations of the edges of the panel strips are given by

$$\left.\begin{aligned} y_j &= \tfrac{1}{2}s\left(1+\cos\left[\frac{(2j-1)\,\pi}{2(M+1)}\right]\right), \\ y_{M+1} &= 0, \end{aligned}\right\} \tag{34}$$

where $j = 1, 2, \ldots, M$ and M is the panel section in the vertical direction. The collocation sections are located at

$$y_j^c = \tfrac{1}{2}s\left(1+\cos\frac{j\pi}{M+1}\right) \quad \text{where} \quad j = 1, 2, \ldots, M. \tag{35}$$

Note that the upper edge of the last panel strip coincides with the waterline, but no collocation section is introduced on the free surface. In view of the condition (13), the collocation sections at the leading edge and lower edge are also omitted.

Since all unknowns are confined within S_b, no collocation point is introduced on the wake. To evaluate the contribution of the wake to the collocation points on S_b numerically, we choose to discretize the wake into panels for simplicity. A simple analysis shows that the contribution of a panel far downstream in the wake to a point upstream converges like $1/R^3$, where R is the distance from the panel to the point. Thus, the semi-infinite wake sheet may be truncated. The results of numerical experiments indicate that the solution changes less than 1 % if a wake sheet of five times the chord length is included in the computation.

To determine the panel edges in the wake, the oscillatory features of the kernel must be taken into account. Based on numerical studies of different components of the kernel function, a half-chord length of the wake immediately after the trailing edge is discretized such that the panels are symmetrical about the trailing edge. This

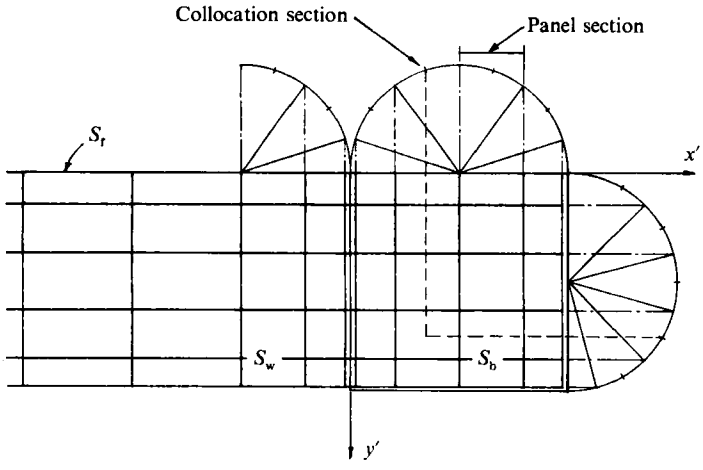

FIGURE 2. Panel and collocation-point arrangement on the submerged lifting surface and its wake based on the present scheme. (Here $x' = x/c$ and $y' = y/s$. The last collocation section in the chordwise direction on S_b coincides with the trailing edge.)

arrangement may help to maintain a similar resolution in evaluating the contribution due to a panel on the wake when compared with that due to a panel on the lifting surface. Also it avoids the numerical difficulty due to an abrupt change in the size of adjacent panels. The size of the panel segments over the remainder of the wake is determined by a prespecified maximum aspect ratio. The scheme of discretization described above is illustrated in figure 2.

If the wake is divided into N_w segments longitudinally, the discrete form of the integral equation may be written as

$$\sum_{j=1}^{M}\left[\sum_{i=1}^{N} m_{ji}\lim_{z\to 0}\frac{\partial}{\partial z}\iint_{\Delta S_{ji}}\frac{\partial}{\partial\zeta}G(\boldsymbol{p}_k;\boldsymbol{q}_{ji})\Big|_{\zeta=0}\mathrm{d}\xi\,\mathrm{d}\eta + \sum_{i=N+1}^{N+N_w} m_{jN}\lim_{z\to 0}\frac{\partial}{\partial z}\iint_{\Delta S_{ji}}\frac{\partial}{\partial\zeta}G(\boldsymbol{p}_k;\boldsymbol{q}_{ji})\Big|_{\zeta=0}\mathrm{d}\xi\,\mathrm{d}\eta\right] = 4\pi U\left(\alpha-\frac{\partial f(x_k,y_k)}{\partial x}\right), \quad (36)$$

where $k = 1, 2, \ldots, N_t$ and $N_t = M \times N$ is the total number of collocation points on the lifting surface, which is also equal to the total number of panels of S_b. ΔS_{ji} is the domain of a generic panel S_{ji} located at the jth panel strip and ith section. The normal of all panels is defined positive in the z-axis direction.

Equation (36) can be written in a standard form for a linear system of equations:

$$\boldsymbol{A}\boldsymbol{m} = \boldsymbol{b}, \quad (37)$$

where $\boldsymbol{A}$ is an $N_t \times N_t$ influence coefficient matrix, $\boldsymbol{m}$ is the unknown N_t-vector containing the unknown dipole strength of each panel on the surface S_b, and $\boldsymbol{b}$ is a known N_t-vector, which is determined by the boundary condition on the lifting surface. Since the panel size is non-uniform and the kernel function is not symmetric in $\boldsymbol{p}$ and $\boldsymbol{q}$, the resulting coefficient matrix $\boldsymbol{A}$ is a non-symmetric, full matrix.

Every element of $\boldsymbol{A}$ is the superposition of integrals of the following canonical form:

$$w_{ji} = \lim_{z\to 0}\frac{\partial}{\partial z}\iint_{\Delta S_{ji}}\frac{\partial}{\partial\zeta}G(\boldsymbol{p}_k;\boldsymbol{q}_{ji})\Big|_{\zeta=0}\mathrm{d}\xi\,\mathrm{d}\eta$$
$$= \lim_{z\to 0}\frac{\partial}{\partial z}\iint_{\Delta S_{ji}} z\left(\frac{1}{r^3}-\frac{1}{r_0^3}\right)\Big|_{\zeta=0}\mathrm{d}\xi\,\mathrm{d}\eta - \iint_{\Delta S_{ji}}\frac{\partial^2 H(\boldsymbol{p}_k;\boldsymbol{q}_{ji})}{\partial\zeta^2}\Big|_{z=0,\zeta=0}\mathrm{d}\xi\,\mathrm{d}\eta, \quad (38)$$

where subscripts k, j, i are defined in (36). Since the singularities contained in the function H are weaker, the z-derivative and the surface integral in (38) have been interchanged. To construct $\boldsymbol{A}$ requires $N_t^2 + NN_w M^2$ evaluations of (38). Thus efficient quadrature for (38) is essential.

The surface integral of the derivative of the Rankine singularities $1/r$ and $1/r_0$ can be evaluated using the algorithm developed by Newman (1986). For simplicity, the contribution from the remaining integral is evaluated by a one-point quadrature at the collocation point of each panel. To evaluate the second normal derivative of the double integral, derivatives are directly applied to the polynomial approximation for the integral itself derived by Newman (1987*a*). Since function H satisfies Laplace equation, the second normal derivative of H can be replaced by the corresponding tangential derivatives on the centreplane. Thus single integral in (14) needs to be evaluated only on the centreplane, where the effective expansions described by Newman (1987*b*) can be used. Following his approach, the single integral is replaced by the sum of the Dawson's integral and a pair of complementary Neumann expansions. The corresponding analytic expressions for the second normal derivatives of these integrals and the effective algorithms are described in Appendices A and B. The approach described above allows the evaluation of the integrals in (38) with uniform accuracy of five significant digits without recourse to numerical integration.

From energy conservation, the drag force acting on the lifting body may be evaluated at the Treftz plane. In general this is not practical because it requires knowledge of the complete wave system generated by the plate. However, in the limiting cases of zero or infinite Froude number, the integration associated with the waves vanishes. Thus, in these cases the drag must be equal to the rate of kinetic energy flux across a transverse plane at the far field. The normalized energy flux is given by

$$C_D^{(2)} = \frac{1}{U^2 S_0} \iint_{-\infty}^{\infty} |\nabla \phi|^2 \, \mathrm{d}y \, \mathrm{d}z.$$

Applying the divergence theorem to this integral and utilizing the Laplace equation, the induced drag evaluated at the far field may be written as

$$C_D^{(2)} = \frac{2}{U^2 S_0} \int_0^s m(0, y) \frac{\partial \phi}{\partial z} \mathrm{d}y, \tag{40}$$

where conditions (12) and (13) are also used in deriving the above expression. If the scheme is converging to the correct solution, the ratio of the near-field and far-field drag coefficients $C_D^{(1)}/C_D^{(2)}$ should converge to 1.

Since the computational time is dominated by the calculation of the matrix $\boldsymbol{A}$ for $N_t > 10^2$, the resulting linear system of algebraic equations is solved by a standard LU factorization routine using Gaussian elimination with partial pivoting. The convergence of the numerical solutions is assumed if the solutions obtained by systematically refining the discretization converge to the same limit for a given Froude number.

4. Numerical results and remarks

The numerical scheme described in the preceding section is validated first at the zero-Froude-number limit by comparison with results in aerodynamic reports. For this purpose, a rectangular planform with aspect ratio $A = 1$ (which will be referred

Panels on S_b	C_L/α	C'_M/α	$C_D^{(1)}/C_L^2$	$C_D^{(1)}/C_D^{(2)}$
5×5	2.4699	−0.5174	0.1531	0.9610
10×10	2.4713	−0.5174	0.1577	0.9901
20×20	2.4714	−0.5174	0.1591	0.9993

TABLE 1. Numerical experiments for convergence using Plate A at $F_n \to 0$, C'_M is the moment with respect to the leading edge

Method	C_L/α	C'_M/α	$C_D^{(1)}/C_L^2$	$C_D^{(1)}/C_D^{(2)}$
Present $N=10, M=10$	2.4713	−0.5174	0.1577	0.9901
QCM $N=8, M=15$	2.4707	−0.5173	0.1595	0.9972
VLM $N=6, M=20$	2.5239	−0.5334	0.1554	0.9747
NLR	2.4744	−0.5182	0.1609	1.0101
Wagner (1966)	2.4778	−0.5180	0.1619	1.0167

TABLE 2. Aerodynamic characteristics of a rectangular wing of $A = 2$ at $M_\infty = 0$

Panels on S_b	C_L/α	C_M/α	$C_D^{(1)}/\alpha^2$	C_T/α^2
6×6	1.7039	−0.2803	1.2956	0.4083
12×12	1.6900	−0.2541	1.2850	0.4050
24×24	1.6550	−0.2476	1.2575	0.3975
48×48	1.6277	−0.2473	1.2327	0.3950

TABLE 3. Numerical experiments for convergence using Plate B at $F_n = 0.8$

to as Plate A) is selected. In this limiting case, the results for Plate A are comparable with those of a rectangular wing of $A = 2$ at zero Mach number ($M_\infty = 0$).

The results of the convergence check are tabulated in table 1. The convergence of solutions is indicated by the agreement of the near-field and far-field induced drags. In this case, the far-field drag coefficient is computed by (40). The present results for the overall aerodynamic characteristics of Plate A are compared to those from other methods including VLM, QCM and some continuous load methods (NLR, cf. Garner, Hewitt & Labrujere 1968; Wagner 1966) in the table 2. For the force distributions, comparisons between the present results and those of thin-wing theory show quantitative agreement, as shown in Xü (1990).

The primary interest of the present work is the finite-Froude-number case. For convenience when comparing with the experiments, a rectangular flat plate of $A = 0.5$ (which will be referred to as Plate B) is selected for numerical computation. Since the solution is assumed linear in α, all the numerical results are normalized by the angle of attack. The global convergence check for the hydrodynamic coefficients is summarized in table 3. The condition number of the influence matrix $\boldsymbol{A}$ is found of the same order as its dimension. Since the matrix $\boldsymbol{A}$ is evaluated with an accuracy of five significant digits, the accuracy of the converged solution is estimated at about two significant digits.

As shown in figure 3, the local convergence near the leading and lower edges is better than that near the waterline and trailing edge. This convergence property is also reflected in figures 4 and 5. In figure 4, the fast convergence of parameter $C(y)$

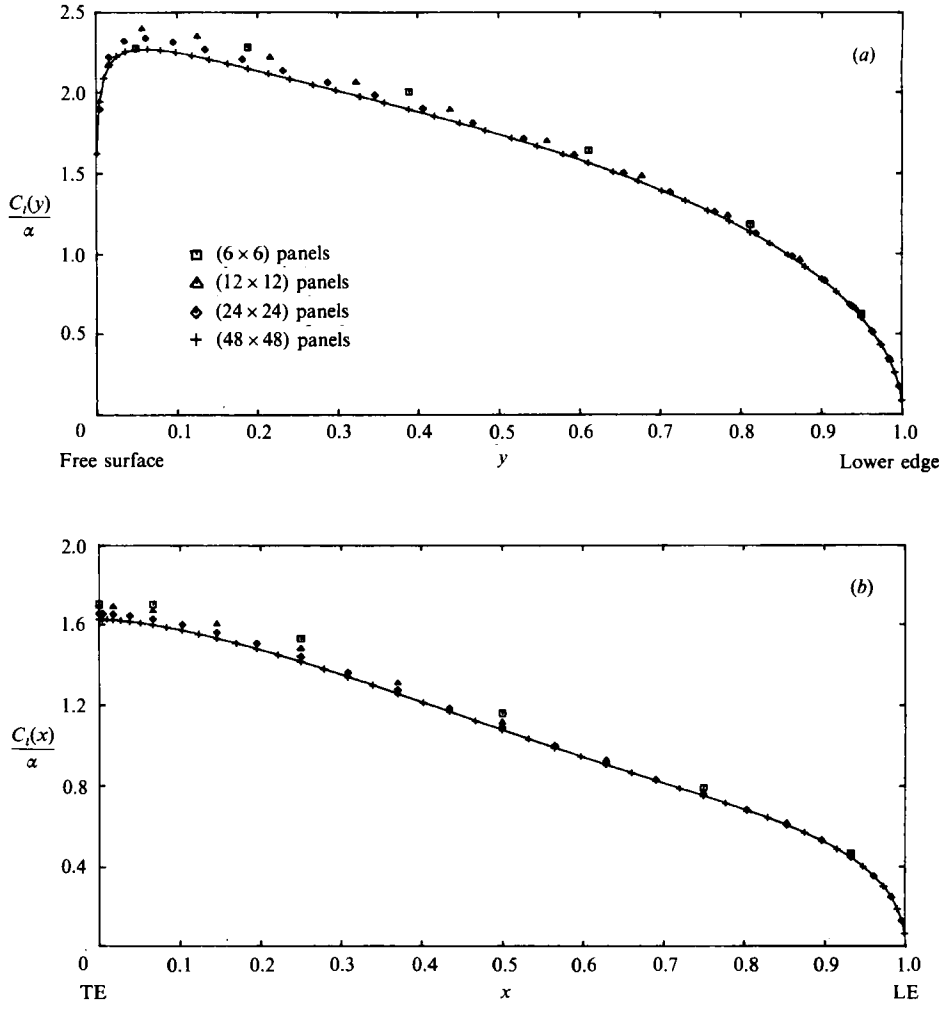

FIGURE 3. Convergence check for the distributed force in (*a*) the spanwise and (*b*) chordwise directions using Plate B at $F_n = 0.8$.

clearly indicates the rapid convergence of the solution near the leading edge. The pressure at the trailing edge is convergent except near the intersection point with the free surface as shown in figure 5, where the pressure coefficients are evaluated by (18). The results in figure 5 indicate that the solution near the intersection point does not satisfy the Kutta condition. For a linearized formulation, this is inevitable, as has been pointed out in §2. It is interesting to note that in the recent visualization test by Maniar, Newman & Xü (1990), a sharp transverse flow accompanying the free-surface jump at the intersection point, contrary to the Kutta condition, has been observed. The distributed drag and moment are also convergent, as shown by Xü (1990).

After establishing the convergence of the algorithm, the hydrodynamic features for a yawed plate can be explored numerically. Since the longitudinal derivative of the potential function is regular in the θ-coordinate defined in (16), the pressure coefficient on the plate can be readily evaluated by (17) with a central-difference formula. The perspective view of the complete pressure distributions for Plate B at

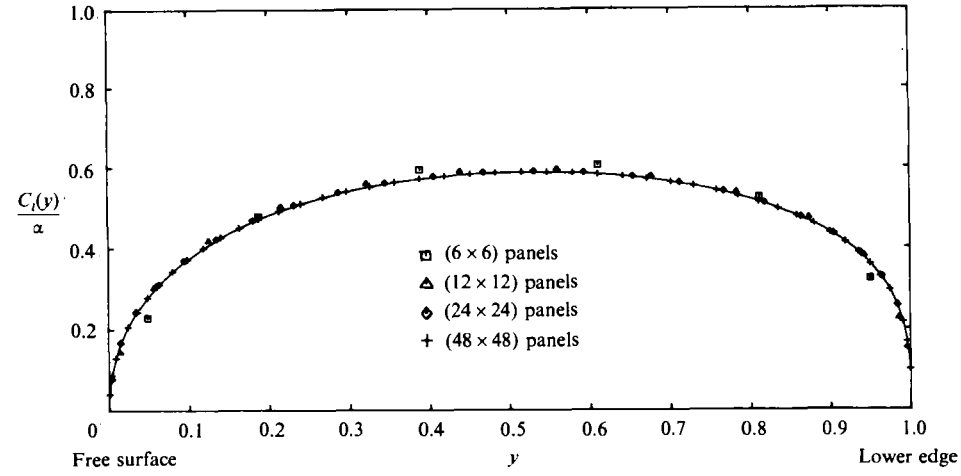

FIGURE 4. Distribution of the strength of the leading-edge singularity at $F_n = 0.8$ for various discretizations.

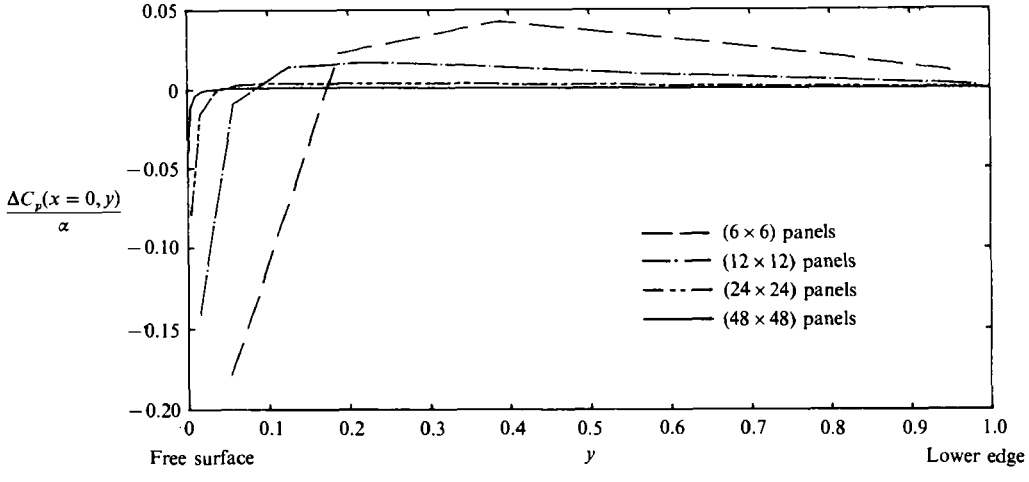

FIGURE 5. Pressure distribution at the trailing edge of Plate B ($F_n = 0.8$) for various discretizations.

various Froude numbers F_n are shown in figure 6, where the domain S_b is normalized in the same manner as in figure 2 and the pressure coefficient is normalized by its value at the mid-span of the first collocation column next to the leading edge. In the two limiting cases of $F_n \to 0$ or ∞, the pressure Kutta condition is satisfied *everywhere* at the trailing edge. At $F_n = 0.3$ and 0.8, the pressure coefficients are non-zero near the intersection point of the free surface and the trailing edge. When $F_n = 0.3$, the free-surface displacement at the intersection point is small, hence the non-uniformity is less pronounced than that at $F_n = 0.8$. In all cases, the non-uniformity is confined within a few panels adjacent to the intersection point, and as the number of panels increases the domain of the non-uniformity decreases.

The free-surface profiles on the plate surface may be readily computed from (31), by extrapolating the pressure coefficient vertically to the waterline. The results are shown for various discretizations at $F_n = 0.3$ and 0.8 in figure 7 (extrapolation at the

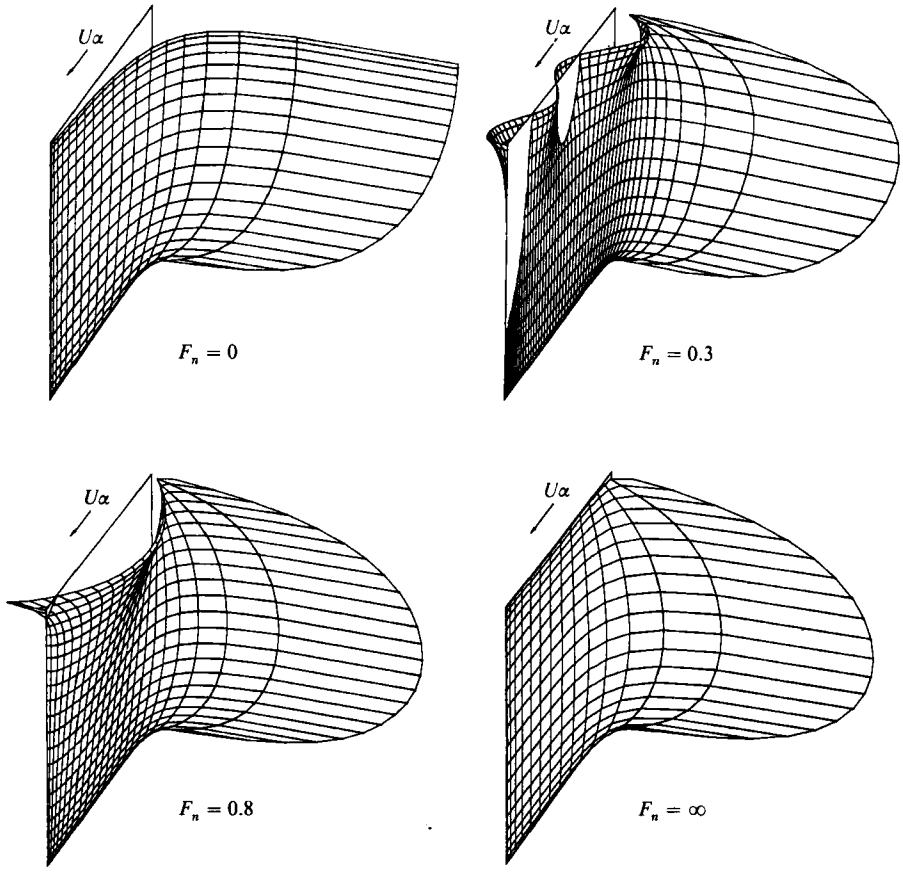

FIGURE 6. Normalized pressure distributions on the submerged portion of Plate B, at the indicated Froude numbers. (The intersections of the grid lines are the locations of the collocation points in the numerical solution. The infinite pressure at the leading edge must be inferred by extrapolation since the first column of the collocation points is downstream of the leading edge.)

leading edge is not accurate where the non-zero η-values must be disregarded). For $F_n = 0.3$, the finer chordwise discretizations have been used to account for the shorter wavelength scale.

The distributions of the hydrodynamic coefficients are presented in figures 8–11 for six selected Froude numbers, from zero to infinity. As shown in the single integral of (14), the intersection point of the leading edge and free surface is an essential singularity which must be excluded from the computation. For non-zero F_n, the pressure on the free surface must be finite. Although it may not be imposed explicitly in the solution scheme, a valid solution must satisfy this condition. As shown in figure 8, the strength of the square-root singularity at the leading edge indeed diminishes towards the waterline. As $F_n \to 0$, a double-body flow results. The intersection point is equivalent to the leading-edge point at mid-span of a thin wing with twice the aspect ratio. Thus the pressure becomes singular again. The parameter $C(y)$, which corresponds to the cross-flow effect at the leading edge, reaches a maximum near the mid-draft, except when $F_n = 0$. This prediction is in agreement with the results of visualization tests of van den Brug *et al.* (1971). The leading-edge separations were reported at half-draft below the still waterline starting as low as

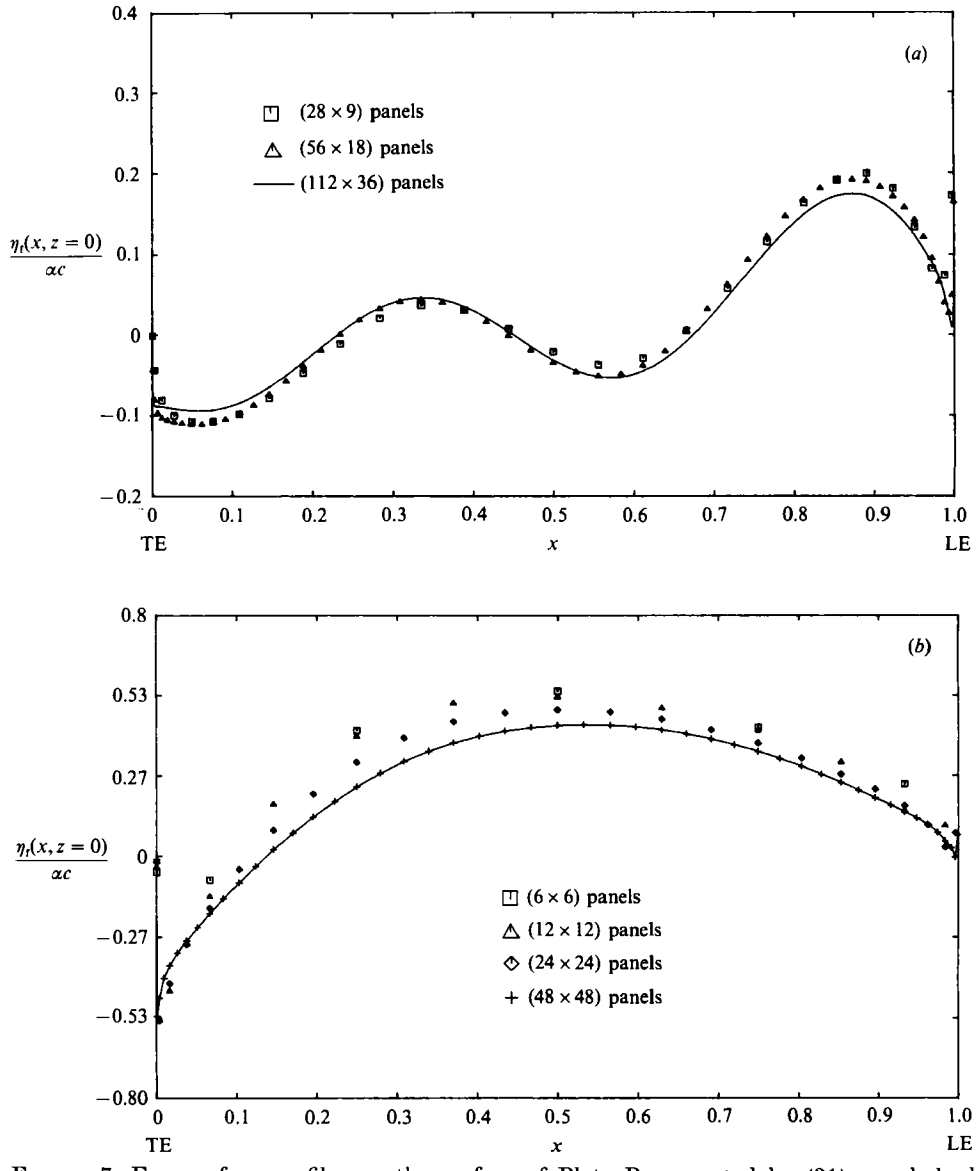

FIGURE 7. Free-surface profiles on the surface of Plate B computed by (31); symbols denote different discretizations of S_b with the indicated numbers of panel segments in the chordwise and spanwise directions: (*a*) $F_n = 0.3$ and (*b*) $F_n = 0.8$.

$\alpha = \tan^{-1} 0.05$. For non-zero Froude numbers, there is no condition which specifies that the trailing vortex vanish on the waterline. Thus, at the waterline the slopes of the spanwise force distributions is non-zero in general. The slopes of the curves shown in figure 11 represent the variation of the integrated spanwise pressure force along the chord. The curve becomes oscillatory as F_n decreases, which corresponds to the decrease of the transverse wavelength. All these curves have zero slopes approaching the trailing edge, which indicate that the pressure Kutta condition is fulfilled.

In figures 12 and 13, the integrated lateral force and yaw moment are compared with the experimental data of van den Brug *et al.* (1971) and with the slender-body theory of Chapman (1976). The agreement between the present results and the

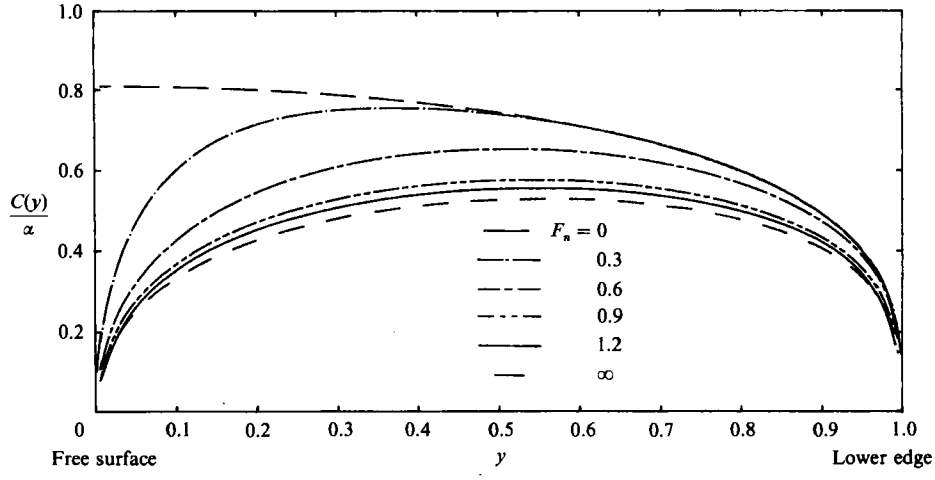

FIGURE 8. Spanwise distributions of the parameter C associated with the leading-edge singularity for Plate B at the indicated Froude numbers.

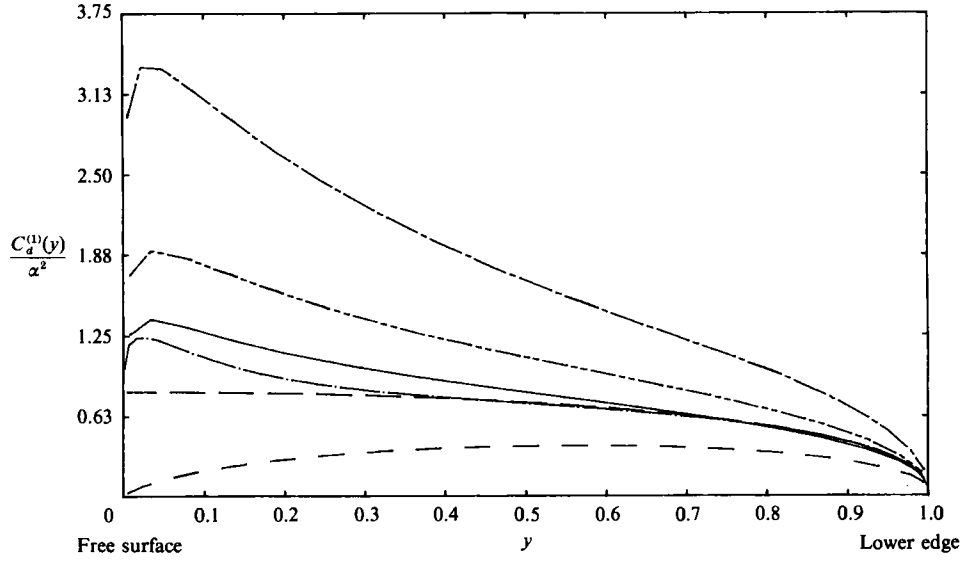

FIGURE 9. Spanwise distributions of the induced-drag coefficient for Plate B at various Froude numbers. Legend as figure 8.

experimental data appears to be satisfactory. At very high F_n, the two numerical results agree. For $F_n < 0.8$, the improved agreement from the present results compared with the slender-body approach is rather obvious. The analytical curves in figures 12, 13 and 14 should approach their zero-Froude-number limits with small oscillations corresponding to the wave forms on the two sides of the plate at a particular Froude number.

The limiting values as $F_n \to 0$ are $C_L/\alpha = 1.4597$, $C_M/\alpha = 0.4865$, $C_T/\alpha^2 = 0.7852$, $C_D^{(1)}/\alpha^2 = 0.6745$; and as $F_n \to \infty$, $C_L/\alpha = 0.6348$, $C_M/\alpha = 0.2599$, $C_T/\alpha^2 = 0.3215$, $C_D^{(1)}/\alpha^2 = 0.3132$. The corresponding limiting values from the slender-body approximation by Chapman (1976) are $C_L/\alpha = \pi$, $C_M/\alpha = \frac{1}{2}\pi$ for $F_n A^{\frac{1}{2}} \to 0$, and $C_L/\alpha = 1.25$, $C_M/\alpha = 0.62$ for $F_n A^{\frac{1}{2}} \to \infty$. The difference between the corresponding limiting values of the two approaches represents the effect of the finite aspect ratio.

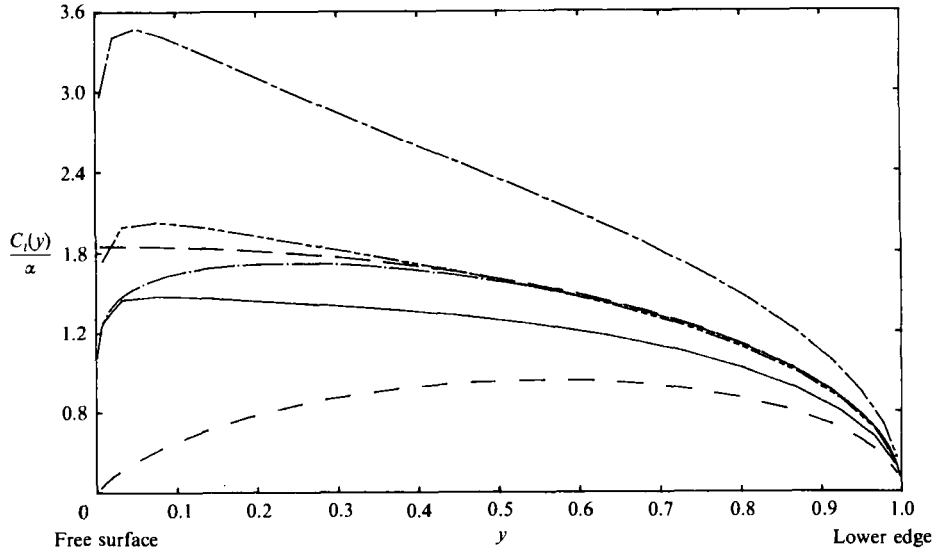

FIGURE 10. Spanwise distributions of the lateral-force coefficient for Plate B at various Froude numbers. Legend as figure 8.

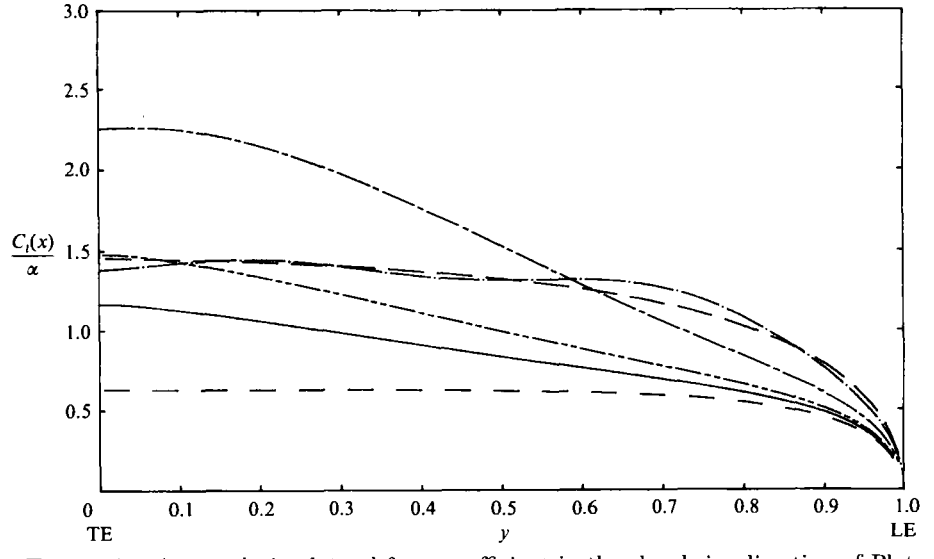

FIGURE 11. Accumulative lateral-force coefficient in the chordwise direction of Plate B at various Froude numbers. Legend as figure 8.

The total drag and leading-edge thrust coefficients are presented in figure 14 as a function of Froude number. It is interesting to note that these two curves cross each other at approximately $F_n = 0.25$. It is also noteworthy that at the zero-Froude-number limit the leading-edge thrust is greater than the wave-induced drag. These results predict that there is a favourable region of Froude number where the leading-edge thrust is large enough to overcome the wave-induced drag. This favourable speed region (which is $0 < F_n \leqslant 0.25$ for a plate with $A = 0.5$) can be determined by performing the present computation for lower Froude numbers.

However, as the Froude number decreases, the wavelength decreases in proportion to F_n^2. The computational time increases as a function of F_n^{-2} for small Froude

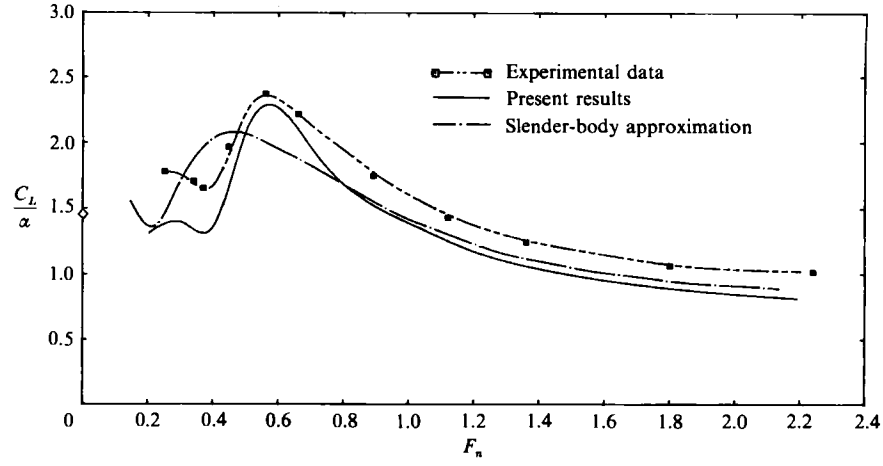

FIGURE 12. Comparison of the lateral-force coefficients of Plate B at various Froude numbers. The experimental data are from van den Brug *et al.* (1971) and the slender-body approximation is due to Chapman (1976). ◇ denotes the present limiting value as $F_n \to 0$.)

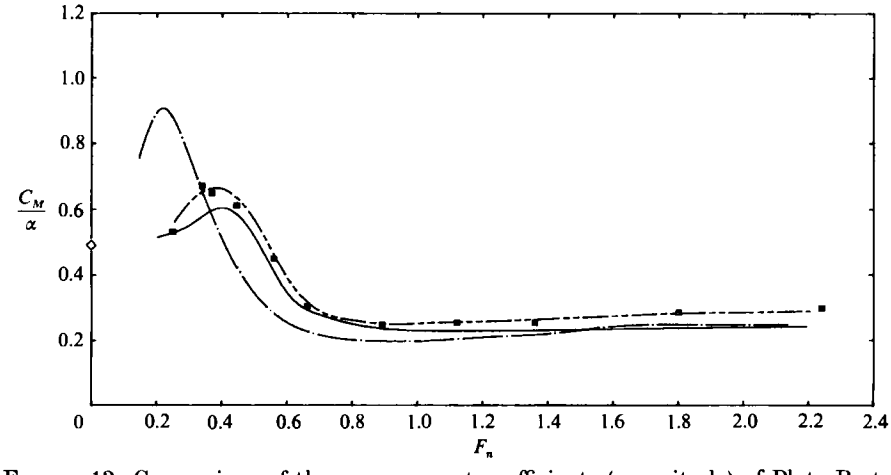

FIGURE 13. Comparison of the yaw-moment coefficients (magnitude) of Plate B at various Froude numbers (the sources of data and legend are the same as in figure 12).

numbers. For instance, if the results for $F_n = 0.8$ obtained by using 144 unknowns are considered acceptable, it takes $4^2 \times 144 = 2304$ unknowns to obtain a similar resolution for $F_n = 0.2$. This estimate has been confirmed in the convergence check at $F_n = 0.2$. The total number of panels on S_b and S_w is as high as $O(10^5)$ for the latter case which takes 1.4 hours of CPU time on a CRAY Y-MP. It is for this reason that the computations were not extended to Froude numbers less than 0.2. The present computations were performed on a VAX/750 for N_t less than 10^3, on a CRAY Y-MP for larger N_t.

The present approach has been extended to include planforms with arbitrary profiles at the leading and trailing edges. In those cases, the panel strips and collocation sections in the vertical direction should be determined first. Then, local chord lengths can be calculated at each section, and the longitudinal panel and collocation sections can be determined. For force calculations, the sectional leading-edge thrust in (21) must be multiplied by $\sec \Lambda(y)$, where $\Lambda(y)$ is the local leading-

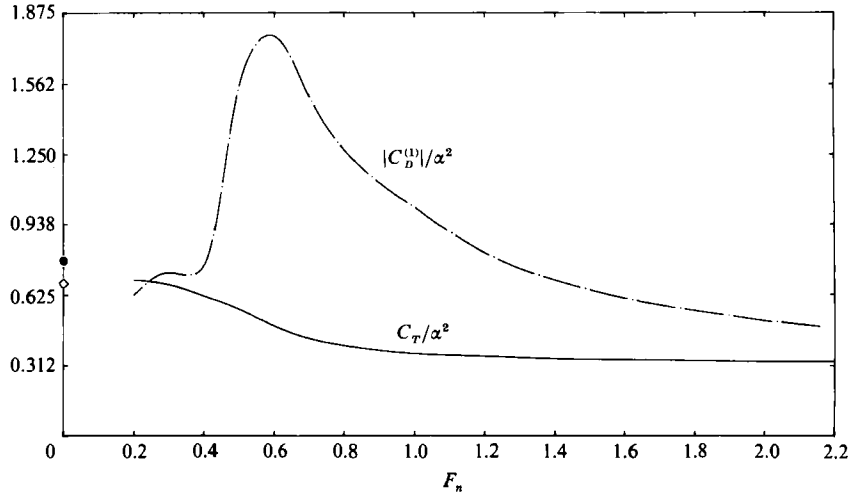

FIGURE 14. The leading edge thrust and drag coefficients (magnitude) by the present method for Plate B at various Froude numbers. (●, ◇ denote the present limiting values of C_T/α^2 and $|C_D^{(1)}|/\alpha^2$ as $F_n \to 0$, respectively.)

Method	C_L/α	C'_M/α	$C_D^{(1)}/C_L^2$	$C_D^{(1)}/C_D^{(2)}$
Present $N = 6, M = 16$	2.7365	−3.0818	0.1137	1.0030
QCM $N = 5, M = 20$	2.7382	−3.0844	0.1143	1.0054
VLM $N = 5, M = 15$	2.7944	−3.1775	0.1055	0.9275
NLR $M = 15$	2.7373	−3.1074	0.1201	1.0564
NLR $M = 31$	2.7576	−3.1155	0.1138	0.9921

TABLE 4. Aerodynamic characteristics of a Warren 12 planform of $A = 2\sqrt{2}$ at $M_\infty = 0$

edge sweep angle of a panel strip, whereas the upper and lower limits of the integrals in the formulae (22)–(27) can be modified in a straightforward fashion to compute the corresponding hydrodynamic coefficients. The results for the Warren 12 planform (aspect ratio $A = 2\sqrt{2}$, leading-edge sweep angle $\Lambda = 53.5°$) are shown in table 4.

5. Conclusions

Within the context of linear potential theory, it has been shown that the steady problem of a yawed surface-piercing plate can be solved through a boundary-integral-equation formulation without restricting the aspect ratio or the Froude number. The convergence of the numerical scheme has been demonstrated both in the zero-Froude-number limit and for a finite Froude number. For a yawed surface-piercing plate of zero thickness, it is found that the discretization scheme is indispensable for the convergence of the solution. It is deduced that in a linearized formulation the pressure Kutta condition and the free-surface condition are not compatible. The numerical results show that the effects due to this incompatibility are confined locally at the intersection point of the free surface and the trailing edge.

Convergent results have been obtained for most of the hydrodynamic parameters of practical importance, which include the integrated lateral force, yaw moment and drag, and their spanwise distributions. Also included are the computed distributions of the strength of the leading-edge singularity. This parameter can be used to predict the occurrence of cavitation and separation of a bow region, and to guide the design of a ship or sailboat.

Comparisons of the present results for force and moment with the experimental data of van den Brug *et al.* gave satisfactory agreement. In the zero-Froude-number limit, the present approach recovers thin-wing theory for an incompressible flow. The convergence rate of the present method is comparable with that of the QCM. At the infinite-Froude-number limit, the solution is also convergent.

It is also found that for a surface-piercing plate there exists a favourable speed region where the wave-induced drag is less than the leading-edge thrust. For a plate of aspect ratio 0.5, it is $F_n \leqslant 0.25$. In an idealized case, if a sailboat is sailing within the favourable speed region, the additional thrust from the leading edge (its bow and keel profile) may be helpful in overcoming its frictional resistance.

Since the free-surface jump phenomenon behind the trailing edge is excluded in a linearized lifting problem, only a nonlinear approach will be appropriate for studies of the jump phenomenon.

The author sincerely thanks Professor J. N. Newman for his valuable guidance and encouragement during the course of this research. The helpful discussions with Professor P. D. Sclavounos and Professor J. E. Kerwin are also gratefully acknowledged. This study was financially supported by the Office of Naval Research, contract No. N00014-88-K-0057. The computations for large system of equations are performed at the Pittsburgh Supercomputer Center.

Appendix A. Evaluation of the second normal derivative of the double integral on the centreplane

The Cartesian coordinates system used by Newman (1987*a*) is defined as follows: the origin is located at the image of the source and the $\bar{x}$-axis is in the direction of forward motion of the source, the $\bar{y}$-axis is transverse, and the $\bar{z}$-axis is vertical and positive downwards. These coordinates are normalized in terms of the wavenumber $K = g/U^2$. In this coordinate system, the normalized Green function $\bar{G}$ is a function of $(\bar{x}, \bar{y}, \bar{z})$ only. The computational form of the double integral can be defined explicitly by

$$D = \frac{2\mathrm{i}}{\pi} \lim_{\epsilon \to 0} \int_{-\pi/2}^{\pi/2} \cos\phi \, \mathrm{d}\phi \int_0^\infty \mathrm{d}k \frac{\mathrm{e}^{-k\bar{z}+\mathrm{i}k|\bar{x}|\sec\phi + k\bar{y}\tan\phi}}{k - \cos^2\phi + \mathrm{i}\epsilon}, \tag{A 1}$$

where the real part of the final complex solution is assumed. It has been shown by Newman that this integral can be replaced by the sum of a singular component D_S, which is associated with the logarithmic singularity in the integral with respect to k near the origin, and the regular remainder D_R. The expansions for D_S and D_R are listed below.

The singular component can be represented by the following expression (Newman 1987*a*, equation 21):

$$\begin{aligned} D_S \approx & -U_1 - \bar{z}U_3 + \bar{y}V_3 - \bar{x}U_2 + \tfrac{1}{2}[-\bar{z}^2U_5 + \bar{y}^2(U_3 + U_5) - \bar{x}^2U_3] \\ & + \bar{y}\bar{z}V_5 - \bar{x}\bar{z}U_4 + \bar{x}\bar{y}V_4 + \tfrac{1}{6}[-\bar{z}^3U_7 - \bar{y}^3(V_5 + V_7) - \bar{x}^3U_4] \\ & + \tfrac{1}{2}[\bar{z}^2\bar{y}V_7 - \bar{z}^2\bar{x}U_6 + \bar{y}^2\bar{z}(U_5 + U_7) + \bar{y}^2\bar{x}(U_4 + U_6) - \bar{x}^2\bar{z}U_5 + \bar{x}^2\bar{y}V_5] + \bar{x}\bar{y}\bar{z}V_6, \end{aligned} \tag{A 2}$$

where
$$U_m = \frac{2\mathrm{i}^m}{\pi}\int_{-\pi/2}^{\pi/2} \cos^m\phi \log v \,\mathrm{d}\phi, \tag{A 3}$$

$$V_m = \frac{2\mathrm{i}^m}{\pi}\int_{-\pi/2}^{\pi/2} \cos^{m-1}\phi \sin\phi \log v \,\mathrm{d}\phi. \tag{A 4}$$

These two families of integrals can be evaluated by the following relations:

$$U_0 = 2\log\left[\frac{R+\bar{x}}{4}\right], \tag{A 5}$$

$$U_1 = -2-\frac{2\bar{z}}{R+\bar{x}} \tag{A 6}$$

and
$$mU_m + (m-1)\,U_{m-2} = L, \tag{A 7}$$

where

$$L = 2\mathrm{i}^m \frac{1\times 1\times 3\ldots(m-3)}{2\times 4\times 6\ldots(m)} - \frac{2^{2-m}}{m}\sum_{k=0}^{[\frac{m-1}{2}]}\binom{m}{k}(-1)^k\,(m-2k)\cos\left((m-2k)\,\alpha\right)\left[\frac{\rho}{R+\bar{x}}\right]^{m-2k}. \tag{A 8}$$

Also,
$$V_m = \frac{2^{2-m}}{m}\sum_{k=0}^{[\frac{m-1}{2}]}\binom{m}{k}(-1)^k\,(m-2k)\sin\left((m-2k)\,\alpha\right)\left[\frac{\rho}{R+\bar{x}}\right]^{m-2k}, \tag{A 9}$$

where symbol $[(m-1)/2]$ in the upper limit of the summation denotes the integer portion of $(m-1)/2$, and $\binom{m}{k}$ is the binomial coefficient, and spherical coordinates (R,θ,α) were introduced such that

$$\bar{x} = R\sin\theta, \quad \bar{z}+\mathrm{i}\bar{y} = \mathrm{e}^{\mathrm{i}\alpha}R\cos\theta = \rho\,\mathrm{e}^{\mathrm{i}\alpha}. \tag{A 10}$$

The regular portion of the double integral can be approximated by a polynomial expansion:

$$D_{\mathrm{R}} = \sum_{i=0}^{16}\sum_{j=0}^{16}\sum_{k=0}^{16} P_{ijk}[f(R)]^i\,[-1+4\theta/\pi]^j\,[2\alpha/\pi]^{2k}, \tag{A 11}$$

where the coefficients P_{ijk} are given in the tables of Newman (1987*a*). The function $f(R)$ in (A 11) is defined separately according to the radial distance to the origin by the following expressions:

$$f(R) = \begin{cases} 2R-1 & \text{if} \quad 0 < R \leqslant 1; \\ \frac{1}{3}(2R-5) & \text{if} \quad 1 \leqslant R \leqslant 4; \\ \frac{1}{3}(R-7) & \text{if} \quad 4 \leqslant R \leqslant 10; \\ 1-20/R & \text{if} \quad 10 \leqslant R < \infty; \end{cases} \tag{A 12}$$

Thus, $D = D_{\mathrm{S}} + D_{\mathrm{R}}$ where D_{S} is included only for domain $0 < R \leqslant 1$.

The relationship between the normalized coordinates $(\bar{x},\bar{y},\bar{z})$ used in (A 1) and the Cartesian coordinates, (x,y,z) defined in §2 of this paper can be expressed by

$$\bar{x} = (x-\xi)K, \quad \bar{y} = -(z+\zeta)K, \quad \bar{z} = (y+\eta)K, \tag{A 13}$$

where (ξ,η,ζ) is the location of a singular point. From this relation, we have

$$\left.\frac{\partial^2 G}{\partial\zeta^2}\right|_{z=0;\,\zeta=0} = K^3\left.\frac{\partial^2\bar{G}}{\partial\bar{y}^2}\right|_{\bar{y}=0}, \tag{A 14}$$

where $K\bar{G} = G$. Furthermore, the second $\bar{y}$-derivative can be related to the differentiations in the spherical coordinate (R, θ, α) by

$$\left.\frac{\partial^2}{\partial \bar{y}^2}\right|_{\bar{y}=0} = \left[g_1 \frac{\partial}{\partial R} + g_2 \frac{\partial}{\partial \theta} + f_3^2 \frac{\partial^2}{\partial \alpha^2}\right]_{\alpha=0}, \tag{A 15}$$

also

$$\left.\frac{\partial}{\partial \bar{y}}\right|_{\bar{y}=0} = \left[f_3 \frac{\partial}{\partial \alpha}\right]_{\alpha=0}, \tag{A 16}$$

where $g_1 = 1/R$, $g_2 = -\tan\theta/R^2$ and $f_3 = 1/R\cos\theta$. Hereinafter, all differentiations with respect to $\bar{y}$ are assumed to be evaluated at $\bar{y} = 0$, and all differentiations with respect to α, θ, R will be evaluated for $\alpha = 0$. The subscripts $\bar{y} = 0$ and $\alpha = 0$ will be omitted for simplicity.

Differentiating both sides of (A 2) twice with respect to $\bar{y}$, and denoting each differentiation by a prime, we obtain

$$\begin{aligned} D_S'' = &-U_1'' - \bar{z}U_3'' + 2V_3' - \bar{x}U_2'' + \tfrac{1}{2}[-\bar{z}^2 U_5'' + 2(U_3 + U_5) - \bar{x}^2 U_3''] \\ &- \bar{x}\bar{z}U_4'' + 2\bar{x}V_4' + \tfrac{1}{6}[-\bar{z}^3 U_7'' - \bar{x}^3 U_4''] + \tfrac{1}{2}(2\bar{z}^2 V_7' - \bar{z}^2 U_6'' + 2\bar{z}(U_5 + U_7) + 2\bar{x}(U_4 + U_6) \\ &- \bar{x}^2 \bar{z}U_5'' + 2\bar{x}^2 V_5'] + 2\bar{x}\bar{z}V_6'. \end{aligned} \tag{A 17}$$

Using (A 5)–(A 9), in conjunction with (A 15) and (A 16), we have

$$U_0'' = \frac{2}{R(R+\bar{x})}, \tag{A 18}$$

$$U_1'' = \frac{2\bar{z}}{R(R+\bar{x})^2} \tag{A 19}$$

and

$$mU_m'' + (m-1)\,U_{m-2}'' = g_2 \frac{\partial L}{\partial \theta} + f_3^2 \frac{\partial^2 L}{\partial \alpha^2}, \tag{A 20}$$

where

$$\frac{\partial L}{\partial \theta} = -\frac{2^{2-m}}{m} \sum_{k=0}^{[\frac{m-1}{2}]} \binom{m}{k} (-1)^k (m-2k)^2 \frac{1}{1+\sin\theta} \left[\frac{\cos\theta}{1+\sin\theta}\right]^{m-2k-1}, \tag{A 21}$$

$$\frac{\partial L^2}{\partial \alpha^2} = -\frac{2^{2-m}}{m} \sum_{k=0}^{[\frac{m-1}{2}]} \binom{m}{k} (-1)^k (m-2k)^3 \left[\frac{\cos\theta}{1+\sin\theta}\right]^{m-2k}. \tag{A 22}$$

Also

$$V_m' = \frac{2^{2-m}}{mR\cos\theta} \sum_{k=0}^{[\frac{m-1}{2}]} \binom{m}{k} (-1)^k (m-2k) \left[\frac{\cos\theta}{1+\sin\theta}\right]^{m-2k}. \tag{A 23}$$

It is straightforward to verify that U_m' and V_m'' all vanish in this case.

The relations (A 18)–(A 23) are valid for arbitrary values of the index m and coordinates $(\bar{x}, 0, \bar{z})$. Thus, the singular component D_S'' can be evaluated to any order by using these formulae.

Relation (A 15) is applied to evaluate the second normal derivative of the regular portion D_R as expressed in (A 11). The results are listed here:

$$\frac{\partial D_R}{\partial R} = \frac{f'(R)}{f(R)} \sum_{i=0}^{16} \sum_{j=0}^{16} (iP_{ij0})\,[f(R)]^i\,[-1+4\theta/\pi]^j, \tag{A 24}$$

$$\frac{\partial D_R}{\partial \theta} = \frac{4/\pi}{4\theta/\pi - 1} \sum_{i=0}^{16} \sum_{j=0}^{16} (jP_{ij0})\,[f(R)]^i\,[-1+4\theta/\pi]^j, \tag{A 25}$$

$$\frac{\partial^2 D_R}{\partial \alpha^2} = 2\left(\frac{2}{\pi}\right)^2 \sum_{i=0}^{16} \sum_{j=0}^{16} P_{ij1}[f(R)]^i\,[-1+4\theta/\pi]^j. \tag{A 26}$$

Therefore, the second-order normal derivative of the double integral $D'' = D''_S + D''_R$ may be evaluated by (A 14) in conjunction with (A 17)–(A 26). The expansion for D''_S is truncated such that D'' can be evaluated with an estimated accuracy of five significant figures everywhere in the plane $\bar{y} = 0$.

Appendix B. Evaluation of the second normal derivative of the single integral on the centreplane

By using the same normalized Cartesian coordinates as introduced in Appendix A, the single integral can be expressed as the real part of the following expression (Newman 1987*b*, equation 1):

$$S = 4\mathrm{i}H(-\bar{x}) \int_{-\pi/2}^{\pi/2} \mathrm{d}\theta \sec^2\theta \exp\left(-\bar{z}\sec^2\theta + \mathrm{i}\bar{x}\sec\theta + \mathrm{i}|\bar{y}|\sec^2\theta\sin\theta\right), \tag{B 1}$$

where $H(-\bar{x})$ is the unit step function which is equal to 1 when $\bar{x}$ is negative and 0 elsewhere.

Considering the real part of the single integral on the centreplane $\bar{y} = 0$, and making a substitution $s = \sec\theta$, it follows that

$$S = -8H(-\bar{x}) \int_0^\infty \frac{s}{(s^2-1)^{\frac{1}{2}}} \mathrm{e}^{-\bar{z}s^2} \sin(s\bar{x})\,\mathrm{d}s \tag{B 2a}$$

$$= -8H(-\bar{x}) f(\bar{x},\bar{z}). \tag{B 2b}$$

Detailed discussion of the analytic properties of the single integral itself can be found in Newman (1987*b*). Since $\bar{z}$ is non-negative by definition, and $f(\bar{x},\bar{z})$ is odd in $\bar{x}$, vanishing on $\bar{x} = 0$ for $\bar{z} > 0$, it is sufficient to assume hereinafter that $\bar{x} > 0$. The singular point $\bar{x} = 0$, $\bar{z} = 0$ must be excluded from the analysis. The centreplane is divided into three complementary subdomains and different expansions were developed in each domain.

For domain $0 < \bar{x} < 10$; $0.028\bar{x}^2 < \bar{z} < 6$, the function $f(\bar{x},\bar{z})$ can be expressed by (Newman 1987*b*, equation 13):

$$f(\bar{x},\bar{z}) = \bar{z}^{(-\frac{1}{2})} F(X) + \sum_{n=0}^{\infty} J_{2n+1}(\bar{x})\, b_n(\bar{z}), \tag{B 3}$$

where $J_n(\bar{x})$ are Bessel functions of the first kind and $F(X)$ is the Dawson's integral (cf. Abramowitz & Stegun 1964) with argument $X = \frac{1}{2}\bar{x}\bar{z}^{(-\frac{1}{2})}$. The coefficients b_n are defined by

$$b_n = \tfrac{1}{2}\mathrm{e}^{-\bar{z}/2}(-1)^n [K_n(\tfrac{1}{2}\bar{z}) + K_{n+1}(\tfrac{1}{2}\bar{z})] - d_n - d_{n+1}, \tag{B 4}$$

where the functions K_n are the modified Bessel functions of the second kind. The coefficients d_n can be calculated by the following relations:

$$d_0 = 0, \tag{B 5}$$

$$d_1 = 1/\bar{z}, \tag{B 6}$$

$$d_{N+1} + \frac{4n}{\bar{z}} d_n - d_{n-1} = \frac{2}{\bar{z}} \quad \text{for} \quad n = 1, 2, \ldots. \tag{B 7}$$

More discussion of the evaluation of the above coefficients can be found in §3 of Newman (1987*b*).

Since the function f must satisfy the Laplace equation $\nabla^2 f = 0$, it follows that

$$f_{\bar{y}\bar{y}} = -(f_{\bar{x}\bar{x}} + f_{\bar{z}\bar{z}}). \tag{B 8}$$

Moreover, it is apparent that $f(\bar{x},\bar{z})$ in (B 2) satisfies the heat equation $f_{\bar{z}} = f_{\bar{x}\bar{x}}$. Thus, (B 8) may be rewritten as

$$f_{\bar{y}\bar{y}} = -(f_{\bar{x}\bar{x}} + f_{\bar{x}\bar{x}\bar{x}\bar{x}}). \tag{B 9}$$

This formula can be applied to the expansions above to obtain the corresponding expansions for the second $\bar{y}$-derivative of f. The second- and fourth-order $\bar{x}$-derivative of the Dawson's integral in the first term of (B 3) can be computed on the basis of the expansions given in the Appendix of Newman (1987*b*) up to six-decimal accuracy. The summation part is

$$\left(\frac{\partial^2}{\partial\bar{x}^2} + \frac{\partial^4}{\partial\bar{x}^4}\right) \sum_{n=0}^{\infty} J_{2n+1}(\bar{x})\, b_n(\bar{z}) = \sum_{n=0}^{\infty} C_n(\bar{x})\, b_n(\bar{z}), \tag{B 10}$$

with

$$C_n(\bar{x}) = J_{2n-3}(\bar{x}) - 2J_{2n-1}(\bar{x}) + J_{2n+5}(\bar{x}), \tag{B 11}$$

where the coefficients b_n can be evaluated by the same algorithm as in (B 4). The Bessel function J_n can be evaluated by backward recursion. To avoid overflow in the evaluation of the coefficients b_n and underflow in the evaluation of the functions C_n for large values of n, both functions are rescaled by a factor determined by the leading behaviour of C_n, that is

$$A_n = \begin{cases} \bar{x} & \text{if} \quad n = 0; \\ \frac{1}{2}\bar{x} & \text{if} \quad n = 1; \\ (\frac{1}{2}\bar{x})^{2n-3}/(2n-3)! & \text{for} \quad n \geqslant 2. \end{cases} \tag{B 12}$$

Numerical experiments show that this scheme is convergent and effective in the domain $0 < \bar{x} < 9$; $0.12\bar{x}^2 < \bar{z} < 6$. The series is truncated when n exceeds the value of $9.4 - \frac{1}{2}\bar{z} + \bar{x}^2/\bar{z}$. If $\bar{x} < 10^{-3}$ in this domain, the maximum n may be set equal to 3.

When $(\frac{1}{7})^2 < \bar{z}/\bar{x}^2 < 0.12$, the above algorithm must be computed by double precision to avoid cancellation errors in the summation. Also, the truncation of the series (B 10) may be made when n exceeds the value of 12. $-\bar{z} + 0.75\bar{x}^2/\bar{z}$, with the maximum value $n = 49$. For each point on the centreplane $(\bar{x},\bar{z})$, the same maximum value n is used to start the backward recursion for the functions C_n. For $\bar{z} < 10^{-5}$, the derivatives of the Dawson's integral are the dominant part and the summation of the Neumann series is negligible.

For smaller values of $\bar{z}/\bar{x}^2$, the above series expansions suffer from cancellation errors and become inaccurate. A complementary asymptotic expansion was developed by Newman (1987*b*) for this region. The corresponding series for evaluating $f(\bar{x},\bar{z})$ is given by (Newman 1987*b*, equation 18):

$$f \approx \bar{z}^{(-\frac{1}{2})} F(X) - \sum_{n=0} \frac{\bar{z}^n}{n!} \left[\tfrac{1}{2}\pi Y_1(\bar{x}) + \frac{1}{\bar{x}}\right]^{(2n)}, \tag{B 13}$$

where Y_n is the Bessel function of the second kind, and the superscript $(2n)$ denotes differentiation of the same order with respect to $\bar{x}$. $F(X)$ is the Dawson integral defined above.

Substituting (B 13) into (B 9), the first two terms are associated with the second and fourth $\bar{z}$-derivatives of the Dawson integral term which can be evaluated in the same way as for the derivatives of the first term in (B 9) to it yields the following result:

$$f_{2,\bar{y}\bar{y}} \approx \sum_{n=0} \frac{\bar{z}^n}{n!} \left[\left(\tfrac{1}{2}\pi Y_1(\bar{x}) + \frac{1}{\bar{x}}\right)^{(2n+2)} + \left(\tfrac{1}{2}\pi Y_1(\bar{x}) + \frac{1}{\bar{x}}\right)^{(2n+4)}\right]. \tag{B 14}$$

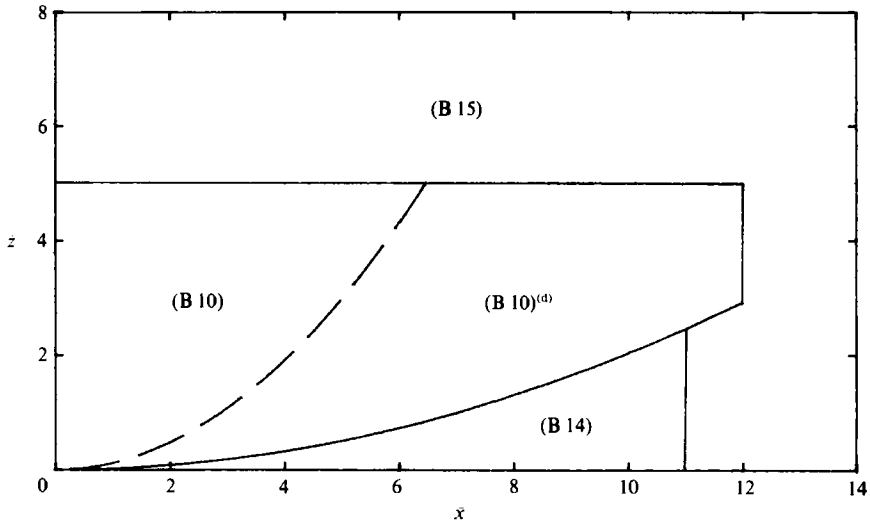

FIGURE 15. Partition of the computational domain for evaluating the second normal derivative of the single integral (cf. Appendix B). The equation numbers in each sub-domain correspond to the expansions derived in Appendix B. The superscript (d) denotes the sub-domain where the expansion must be evaluated with double-precision (if the machine uses 4-byte single-precision numbers). Two parabolic lines are defined by $z = 0.12x^2$ (dashed line) and $z = (x/7)^2$ (solid line).

The terms in this series can be evaluated recursively by the same relation as relation (19) of Newman (1987*b*).

When $(\bar{x}, \bar{z})$ are far away from the origin, the steepest-descent expansion is more effective. The second $\bar{y}$-derivative of function $f(\bar{x}, \bar{z})$ (set $t = \tan\theta$) is

$$f_{\bar{y}\bar{y}} = -\int_0^\infty e^{-\bar{z}(1+t^2)} \sin\left[\bar{x}(1+t^2)^{\frac{1}{2}}\right](t^2+t^4)\,dt. \qquad \text{(B 15)}$$

The minus sign and last factor in the integrand are the only modifications from the original function resulting from the differentiation. Hence, the steepest-descent algorithm (Newman 1987*b*, §5) is modified to compute $f_{\bar{y}\bar{y}}$ for the rest of the domain with an absolute accuracy of five significant digits (cf. Xü 1990).

Finally, the matching boundaries between the different domains where the above expansions are used are determined to ensure that the second $\bar{y}$-derivative of the single integral can be evaluated with a uniform accuracy of five significant figures over the centreplane. These partitions are indicated in figure 15.

REFERENCES

ABRAMOWITZ, M. & STEGUN, I. A. 1964 *Handbook of Mathematical Functions with Formulas, Graphs, and Mathematical Tables.* Washington and New York: Government Printing Office.

BRUG, J. B. VAN DEN, BEUKELMAN, W. & PRINCE, G. J. 1971 Hydrodynamic forces on a surface piercing flat plate. *Rep.* NR 325. Shipbuilding laboratory, Delft University of Technology.

CHAPMAN, R. B. 1976 Free surface effects for yawed surface piercing plates. *J. Ship Res.* **20**, 125–136.

DAOUD, N. 1973 Force and moments on asymmetric and yawed bodies on a free surface. Ph.D. thesis, University of California, Berkeley.

GARNER, H. C., HEWITT, B. L. & LABRUJERE, T. E. 1968 Comparison of three methods for the evaluation of subsonic lifting-surface theory. *Aero. Res. Counc., R & M* 3597.

HIRATA, M. H. 1975 The flow near the bow of a steadily turning ship. *J. Fluid Mech.* **71**, 283–291.

HOUGH, G. R. 1973 Remarks on the vortex-lattice methods. *J. Aircraft* **10**, 314–317.

KERN, E. C. 1973 Wave effects of a free surface piercing hydrofoil. Ph.D. thesis, Department of Ocean Engineering, Massachusetts Institute of Technology.

LAN, C. E. 1974 A quasi-vortex-lattice method in thin wing theory. *J. Aircraft* **11**, 518–527.

MANIAR, H., NEWMAN, J. N. & XÜ, H. 1990 Free-surface effects on a yawed surface-piercing plate. *Proc. 18th Symp. on Naval Hydrodynamics. Ann Arbor, Michigan.*

MICHELL, J. H. 1989 The wave resistance of a ship. *Phil. Mag.* (5) **45**, 106–123. (Also in *The Collected Mathematical Works of J. H. and A. G. M. Michell*, pp. 124–141. Nordhoff, Groningen, 1964.)

NEWMAN, J. N. 1961 Derivation of the integral equation for a rectangular lifting surface. Unpublished.

NEWMAN, J. N. 1973 Flow near the leading edge of a rectangular wing of small aspect ratio with application to the bow of a ship. *J. Engng Maths* **7**, 163–172.

NEWMAN, J. N. 1986 Distributions of sources and normal dipoles over a quadrilateral panel. *J. Engng Maths* **20**, 113–126.

NEWMAN, J. N. 1987*a* Evaluation of the wave resistance Green function Part 1. – The double integral. *J. Ship Res.* **31**, 79–90.

NEWMAN, J. N. 1987*b* Evaluation of the wave resistance Green function Part 2. – The single integral on the centerplane. *J. Ship Res.* **31**, 145–150.

WAGNER, S. 1966 On the singularity methods of subsonic lifting surface theory. *J. Aircraft* **6**, 549–558.

XÜ, H. 1990 Linearized potential flow solution for a yawed surface-piercing plate. S. M. thesis, Department of Ocean Engineering, Massachusetts Institute of Technology.